

# Nanoagents Based on Poly(ethylene glycol)-*b*-Poly(L-thyroxine) Block Copolypeptide for Enhanced Dual-Modality Imaging and Targeted Tumor Radiotherapy

Xiaolei Gu, Zhehong Zhu, Qianyi Fan, Yaohua Wei, Guanglin Wang, Fenghua Meng, Zhiyuan Zhong,\* and Chao Deng\*

Future healthcare requires development of novel theranostic agents that are capable of not only enhancing diagnosis and monitoring therapeutic responses but also augmenting therapeutic outcomes. Here, a versatile and stable nanoagent is reported based on poly(ethylene glycol)-*b*-poly(L-thyroxine) (PEG-PThy) block copolypeptide for enhanced single photon emission computed tomography/computed tomography (SPECT/CT) dual-modality imaging and targeted tumor radiotherapy in vivo. PEG-PThy acquired by polymerization of L-thyroxine-*N*-carboxyanhydride (Thy-NCA) displays a controlled  $M_n$ , high iodine content of  $\approx 49.2$  wt%, and can spontaneously form 65 nm-sized nanoparticles (PThyN). In contrast to clinically used contrast agents like iohexol and iodixanol, PThyN reveals iso-osmolality, low viscosity, and long circulation time. While PThyN exhibits comparable in vitro CT attenuation efficacy to iohexol, it greatly enhances in vivo CT imaging of vascular systems and soft tissues. PThyN allows for surface decoration with the cRGD peptide achieving enhanced CT imaging of subcutaneous B16F10 melanoma and orthotopic A549 lung tumor. Taking advantages of a facile iodine exchange reaction,  $^{125}\text{I}$ -labeled PThyN enables SPECT/CT imaging of tumors and monitoring of PThyN biodistribution in vivo. Besides,  $^{131}\text{I}$ -labeled and cRGD-functionalized PThyN displays remarkable growth inhibition of the B16F10 tumor in mice (tumor inhibition rate  $> 89\%$ ). These poly(L-thyroxine) nanoparticles provide a unique and versatile theranostic platform for varying diseases.


## 1. Introduction

The future healthcare requires development of novel theranostic agents that are capable of not only enhancing diagnosis and monitoring therapeutic responses but also augmenting therapeutic outcomes.<sup>[1]</sup> Dual and multimode imaging techniques capable of affording complementary anatomic, physiological, and molecular information have been recently exploited as innovative strategies to acquire more precise, efficient, and robust diagnosis of various diseases.<sup>[2]</sup> Especially, single photon emission computed tomography/computed tomography (SPECT/CT) yielding anatomic structure information via CT and functional information via SPECT has been identified as a powerful and noninvasive strategy for efficient and fast diagnosis of various cancers and cardiovascular diseases.<sup>[3]</sup> Mostly, radionuclides like  $^{99\text{m}}\text{Tc}$ ,  $^{177}\text{Lu}$ , and  $^{125}/^{131}\text{I}$  are required to acquire SPECT images of targeted organ or disease sites, while no contrast agent is needed if CT imaging is employed only for skeleton location. For example, radioactive  $^{99\text{m}}\text{Tc}$  and  $^{131}\text{I}$  have been intensively employed in the clinics

as contrast agents to noninvasively diagnose ischemic coronary artery diseases,<sup>[4]</sup> evaluate the residual, recurrence, and metastases of differentiated thyroid cancers,<sup>[5]</sup> and visualize the sentinel node location in breast cancer and melanoma prior to operation to facilitate its planning and execution.<sup>[6]</sup> Nanoagents with fascinating physiochemical properties, elevated diagnostic window, and lesion targetability have emerged as superior alternatives to acquire elegant imaging of soft tissues including solid tumors and atherosclerosis.<sup>[7]</sup> For example,  $^{99\text{m}}\text{Tc}$  labeled  $\text{Bi}_2\text{S}_3$ ,  $\text{Cu}_{2-x}\text{Se}$  and Au nanoparticles as SPECT/CT probes have exhibited significantly improved sensitivity and accuracy for 4T1 tumor xenografts<sup>[8]</sup> and vulnerable atherosclerosis plaques.<sup>[9]</sup> Small PEG-EuOF: $^{153}\text{Sm}$  nanocrystals ( $\approx 5$  nm) containing radioactive  $^{153}\text{Sm}$  and high atomic number Eu exhibited long blood retention time and was successfully applied for lymph node CT imaging owing to the remarkable spatial resolution and hypersensitivity.<sup>[10]</sup>  $^{99\text{m}}\text{Tc}$  and gold nanoparticles have often

Dr. X. L. Gu, Z. H. Zhu, Q. Y. Fan, Y. H. Wei, Prof. F. H. Meng, Prof. Z. Y. Zhong, Prof. C. Deng  
Biomedical Polymers Laboratory, and Jiangsu Key Laboratory of Advanced Functional Polymer Design and Application  
College of Chemistry, Chemical Engineering and Materials Science and State Key Laboratory of Radiation Medicine and Protection  
Soochow University  
Suzhou 215123, China  
E-mail: zyzhong@suda.edu.cn; cdeng@suda.edu.cn

Dr. G. L. Wang  
School of Radiation Medicine and Protection and School for Radiological and Interdisciplinary Sciences  
Medical College of Soochow University  
Suzhou 215123, China

 The ORCID identification number(s) for the author(s) of this article can be found under <https://doi.org/10.1002/smll.201902577>.

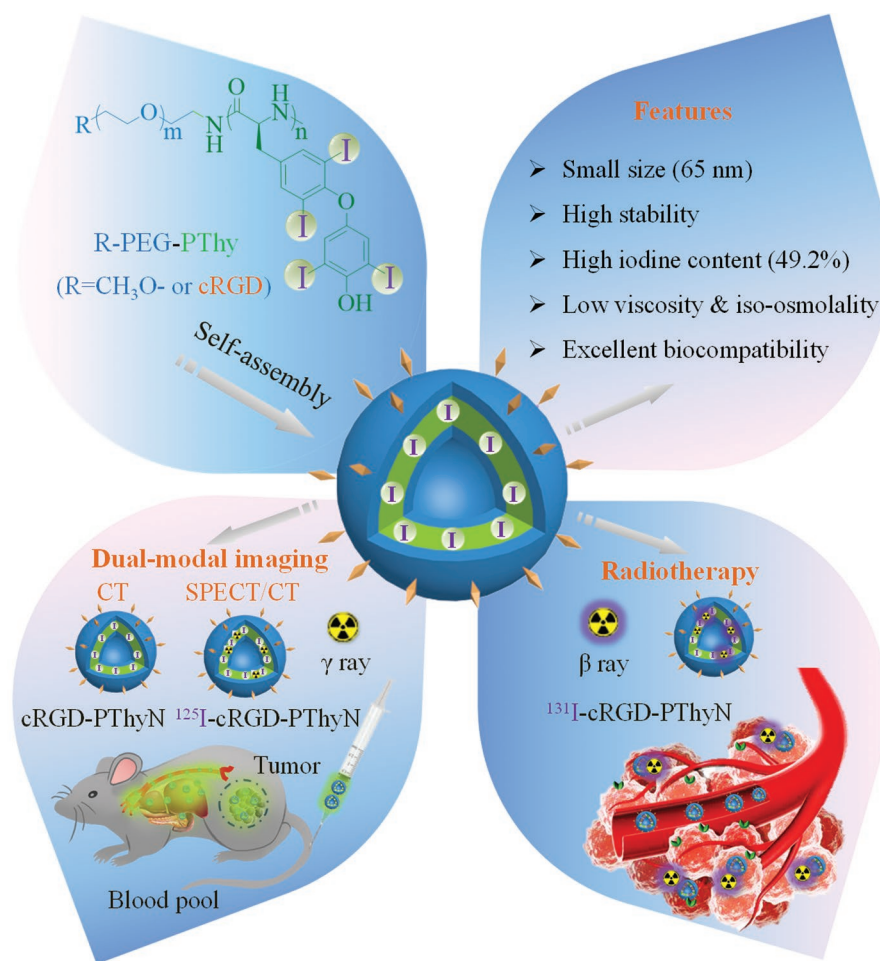
DOI: 10.1002/smll.201902577

been integrated in polyethylenimine and poly(amidoamine) dendrimer-based nanocarriers to form nanoagents, affording highly efficient SPECT/CT dual-model imaging of subcutaneous ovarian tumor and orthotopic hepatic carcinoma models within several hours.<sup>[11]</sup> Although the advanced multifunctional nanoagents have exhibited significantly improved resolution of diagnostic imaging, their clinical translation still encounters many challenges like tedious conjugation, unstable encapsulation, requirement of two and more imaging elements, and potential toxicity of inorganic nanoparticles.

Radiotherapy as a powerful tool has been routinely employed to treat different cancers in the clinics; however, the therapeutic efficacy is frequently compromised by no-selective augmentation and off-targeted systemic side effects. Nanoparticles containing high-Z elements have been recently exploited to achieve enhanced cancer radiotherapy due to facile functionalization, tumor targetability, and high stability.<sup>[12]</sup> For example, radioactive <sup>131</sup>I-doped copper sulfide nanoparticles and albumin nanoparticles with high stability exhibited high accumulation at tumor sites and retarded growth of subcutaneous 4T1 and MDA-MB-231 tumors.<sup>[13]</sup> Gold nanoparticles with high X-ray absorption coefficient often induce increased radiation dose deposited in tissues, and have emerged as potent radiosensitizers in the

treatment of numerous tumors, inducing obvious inhibition of tumor growth and prolonged animal survival.<sup>[14]</sup> However, these nanoagents are challenged by poor biocompatibility and lack of targeting specificity.

In this paper, we designed biocompatible and stable nanoagents (PThyN) based on PEG-PThy for versatile SPECT/CT dual modality imaging and targeted tumor radiotherapy in vivo (**Scheme 1**). PEG-PThy copolypeptides can be simply prepared through controlled polymerization of Thy-NCA that was obtained by cycloaddition of L-thyroxine with triphosgene. Thyroxine, is tyrosine-based amino acid produced by thyroid gland and has been formulated to treat hypothyroidism.<sup>[15]</sup> Thyroxine possessing a high iodine content of over 65 wt% would offer PThyN a high CT contrast ability. Moreover, the iodine of thyroxine could be easily substituted with radioactive <sup>125</sup>I and <sup>131</sup>I, facilitating SPECT/CT dual modality imaging and cancer radiotherapy, respectively. <sup>131</sup>I has been widely used for radioisotope therapy as it emits high-energy  $\beta$  particles that can cause cell DNA strand breaks and therefore cell death.<sup>[16]</sup> The pendant phenyl groups of PThy presenting strong  $\pi$ - $\pi$  stacking might afford PThyN with superior stability. Synthetic polypeptides featured with excellent biocompatibility, in vivo degradability, and unique hierarchical assembly have appeared exceptional



**Scheme 1.** Schematic illustration of nanoagents based on poly(ethylene glycol)-*b*-poly(L-thyroxine) (PEG-PThy) block copolypeptide for versatile SPECT/CT dual-modality imaging and targeted tumor radiotherapy in vivo.

nanovehicles for the diagnosis and therapy of various diseases.<sup>[17]</sup> Here, we report for the first time on development of polypeptide-based theranostic nanoagents capable of versatile SPECT/CT dual imaging and targeted radiotherapy of tumors in mice.

## 2. Results and Discussion

### 2.1. Synthesis of Thy-NCA Monomer and PEG-PThy Copolymers

Thy-NCA was simply obtained as a faint yellow solid in a high yield of 80% through cyclization of L-thyroxine using triphosgene in tetrahydrofuran (THF) (Scheme S1, Supporting Information). The structure of Thy-NCA was corroborated by clear signals at  $\delta$  9.15 owing to amide proton,  $\delta$  4.79 to methine proton, and  $\delta$  2.98–3.08 to the methylene protons in  $^1\text{H}$  NMR (Figure S1, Supporting Information). In addition, the complete shift of methine proton signal of L-thyroxine from  $\delta$  4.18 to  $\delta$  4.79 signified the entire conversion of amino acid into Thy-NCA monomer.  $^{13}\text{C}$  NMR spectrum demonstrated characteristic signals of Thy-NCA at  $\delta$  170.99 and 151.37 attributing to C=O carbon atoms, also two alkane carbons at  $\delta$  58.35 and 35.15 as well as carbon atom adjacent to phenolic hydroxyl group at  $\delta$  150.57 (Figure S2, Supporting Information). Moreover, Thy-NCA revealed a melting point of 240.8–241.6 °C, and a high purity of 98% as characterized by HPLC (Figure S3, Supporting Information). The contents of C, H, and N measured by elemental analysis were close to those calculated for Thy-NCA, and the mass of Thy-NCA assessed via ESI-MS was exactly 802.6. Thus, Thy-NCA monomer has been successfully acquired with a defined structure and high yield.

mPEG-PThy copolymers were synthesized by controlled polymerization of Thy-NCA monomer using mPEG-NH<sub>2</sub> ( $M_n = 3.0 \text{ kg mol}^{-1}$ ) as an initiator. The NCA polymerization was tracked by monitoring the changes of peaks at 1850 and 1785  $\text{cm}^{-1}$  attributed to the carboxyl groups of Thy-NCA using FT-IR measurement, and the results showed that the NCA signals almost completely disappeared within 48 h (Figure S4, Supporting Information). Three days were selected for Thy-NCA polymerization to guarantee complete polymerization. The structure of mPEG-PThy was verified by characteristic signals of PEG ( $\delta$  3.24, 3.51) and PThy ( $\delta$  9.24, 7.66, 7.12, 4.15) in  $^1\text{H}$  NMR (Figure S5, Supporting Information). By comparing the intensities of signals at  $\delta$  3.51 (methylene of PEG) and  $\delta$  4.15 (methine of PThy), the degree of polymerization (DP) of PThy was calculated to be 11, corresponding to an  $M_n$  of 8.3  $\text{kg mol}^{-1}$  (Table S1, Supporting Information). PEG-PThy with a molecular weight of 3.0–8.4  $\text{kg mol}^{-1}$  was selected to acquire comparable iodine content to clinically used iohexol ( $\approx 49 \text{ wt\%}$ ) for CT imaging. GPC measurement revealed that mPEG-PThy had a narrow distribution ( $M_w/M_n = 1.08$ ) and an  $M_n$  of 10.6  $\text{kg mol}^{-1}$ , in close proximity to that (11.3  $\text{kg mol}^{-1}$ ) determined by  $^1\text{H}$  NMR (Figure S6, Supporting Information). Mal-PEG-PThy obtained in a similar way by using Mal-PEG-NH<sub>2</sub> ( $M_n = 4.0 \text{ kg mol}^{-1}$ ) as an initiator also exhibited a controlled  $M_n$  of 10.7  $\text{kg mol}^{-1}$  and an  $M_w/M_n$  of 1.10 (Figure S6, Supporting Information). Through Michael-type addition reaction, cRGDFc was readily conjugated to the terminus of

Mal-PEG-PThy to generate cRGD-PEG-PThy.  $^1\text{H}$  NMR spectrum (Figure S7, Supporting Information) showed characteristic signals belonging to PEG ( $\delta$  3.51), PThy ( $\delta$  9.24, 7.66, 7.12, 4.15), and cRGD ( $\delta$  7.32), verifying the structure of cRGD-PEG-PThy. The  $M_n$  of PThy block in cRGD-PEG-PThy was calculated to be 7.6  $\text{kg mol}^{-1}$  from  $^1\text{H}$  NMR (Table S1, Supporting Information). The degree of cRGD conjugation was determined, using the 9, 10-phenanthraquinone method (Figure S8, Supporting Information),<sup>[18]</sup> to be 90%. mPEG-PThy exhibited an  $\alpha$ -helical structure as indicated by characteristic peaks at 206 and 218 nm in CD spectrum (Figure S9, Supporting Information). SEM images disclosed that PEG-PThy films while keeping intact in Tris-HCl buffer, revealed a significantly broken morphology within 72 h in the presence of proteinase K (Figure S10, Supporting Information), signifying their enzymatic degradability.

### 2.2. Formation and Characterization of PThyN

PThyN was prepared by solvent exchange technique from PEG-PThy copolymers with a PThy block of 8.3  $\text{kg mol}^{-1}$ , corresponding to a high iodine content of 49.2 wt%, which was higher than mostly reported iodinated polymeric nanoparticles used as contrast agents (around 30 wt%).<sup>[19]</sup> Of note, iohexol and iodixanol, small molecular contrast agents currently used in clinic have iodine contents of 46.4 and 49.1 wt%, respectively. PThyN displayed a small size ( $\approx 65 \text{ nm}$ ) and low polydispersity ( $\text{PDI} = 0.11$ ) as characterized by dynamic light scattering (DLS) (Figure 1A; Figure S11, Supporting Information). TEM measurements revealed that PThyN possessed vesicle structure and spherical morphology (Figure 1A). Atomic force microscopy (AFM) image showed that PThyN had a spherical morphology (Figure 1B), and an average height of  $\approx 6 \text{ nm}$  that was over tenfold lower than the diameter (Figure 1C), further signifying their vesicle structure. Importantly, PThyN demonstrated excellent colloidal stability with negligible size change against 100-fold dilution and 10% fetal bovine serum (FBS) (Figure 1D). The high colloidal stability of PEG-PThy nanoparticles might derive from the strong  $\pi$ - $\pi$  stacking, as observed in micelle systems containing catechin, tyrosine, and phenyl moieties.<sup>[20]</sup>

For CT imaging, high concentrations of contrast agents generally are required in order to acquire high contrast and diagnosis accuracy. Interestingly, PThyN as a novel contrast agent revealed a low and concentration-independent osmolality of around 290  $\text{mmol kg}^{-1}$  at varying iodine concentrations of 20–50  $\text{mg I mL}^{-1}$  (Figure 1E), which was close to PBS and blood plasma.<sup>[21]</sup> In contrast, iohexol and iodixanol showed a significantly increased osmolality with elevating concentrations, in which iohexol induced a hardly tolerable osmolality of 386  $\text{mmol kg}^{-1}$  at an iodine concentration of 50  $\text{mg mL}^{-1}$ . Meanwhile, PThyN displayed a low and clinically viable viscosity of 4–5  $\text{mPa s}$  at iodine concentrations ranging from 0–50  $\text{mg mL}^{-1}$ , in sharp contrast with the swiftly elevated viscosity of iohexol and iodixanol with concentrations (Figure 1F). Excessive osmolality and viscosity derived small iodinated contrast agents at high concentrations have been reported to often cause anaphylaxis, arrhythmia, nephrotoxicity, and vasovagal responses.<sup>[22]</sup> These results imply that PThyN with high iodine

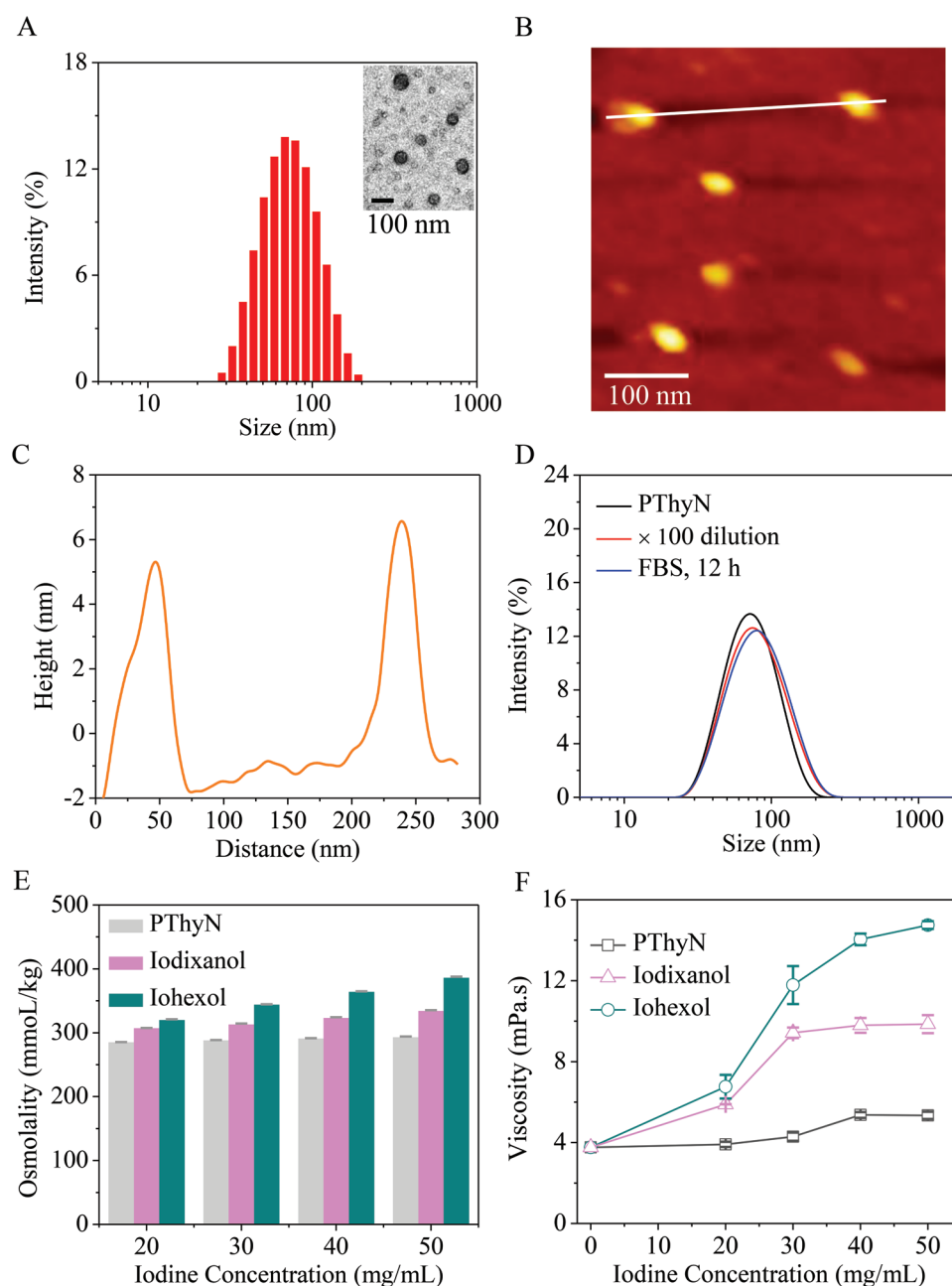


**Figure 1.** Physico-chemical characteristics of PThyN formed from mPEG-PThy copolymers. Size and morphology measured by A) DLS as well as TEM, and B) AFM; C) cross-sectional height profile along the line in inset (B); D) colloidal stability against dilution and 10% FBS; E) osmolality at varying concentrations; and F) viscosity at varying concentrations.

content, low viscosity, and iso-osmolality might be superior and safer alternatives to clinical used small molecular contrast agents.

### 2.3. In Vitro and In Vivo Biocompatibility of PThyN

The biocompatibility and systematic toxicity of PThyN as contrast agents are big concerns for their practical applications considering that diagnosis agents are often employed for disease screening among healthy populations. 3-(4,5-dimethylthiazol-2-yl)-2,5-diphenyl tetrazolium bromide (MTT) assay revealed

that normal cells (L929 cells) and cancer cells (B16F10 cells) following the incubation with PThyN for 48 h at concentrations of 0.1–2.0 mg mL<sup>-1</sup> (around 0.05–1.0 mg I mL<sup>-1</sup>) revealed over 90% cell viability (Figure 2A), signifying that PThyN has negligible cytotoxicity. In contrast, commercial available Fenestra VC and widely explored iodinated nanoemulsions were reported to cause nearly complete cell death at a concentration of around 1.0 mg I mL<sup>-1</sup> following 24 h incubation with cells like HeLa, A431 epithelial carcinoma cells, and BNL-CL2 hepatocytes.<sup>[23]</sup> Hematological assessment revealed that mice following intravenous injection with PThyN at a single dose of 500 mg I equiv. per kg

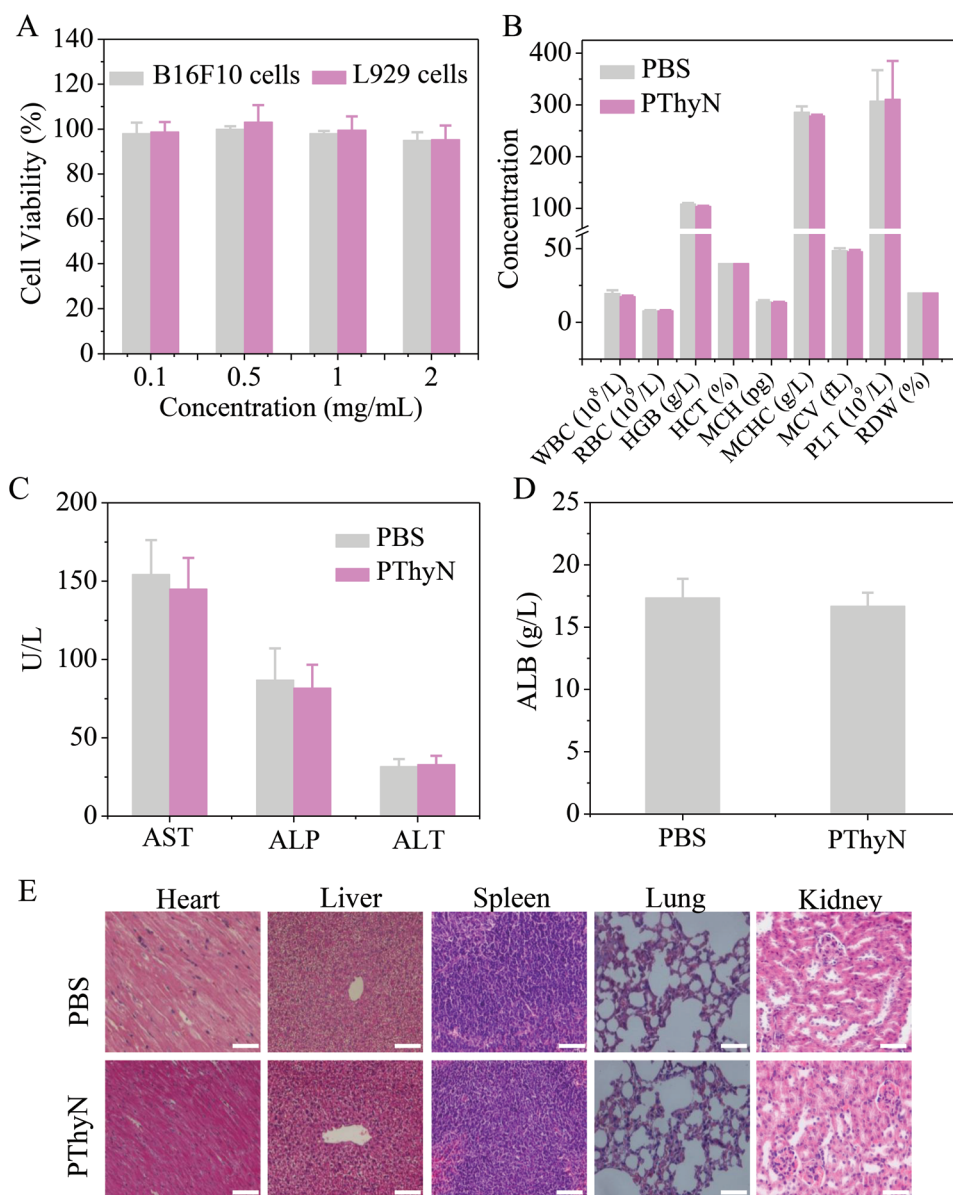


**Figure 2.** Biocompatibility assessment of PThyN. A) Cytotoxicity towards L929 and B16F10 cells determined by MTT assays. The cells were incubated with PThyN for two days ( $n = 4$ ); B) blood and C,D) biochemistry analysis of Balb/c mice after intravenous administration of PThyN at a single dose of 500 mg I equiv. per kg for two days; E) histological evaluation of the heart, liver, spleen, lung, and kidney of mice treated with PThyN at a single dose of 500 mg I equiv. per kg for two days (40 $\times$ ). Scale bar: 200  $\mu$ m.

for two days had equivalent levels of white blood cells (WBC), red blood cells (RBC), hemoglobin (HGB), hematocrit (HCT), mean corpuscular hemoglobin (MCH), mean corpuscular hemoglobin concentration (MCHC), mean corpuscular volume (MCV), platelets (PLT), red cell distribution width (RDW), and mean platelet volume (MPV) to PBS (Figure 2B). Mice treated with PThyN demonstrated equivalent level of kidney function marker albumin (ALB), and liver function markers including aspartate aminotransferase (AST), alkaline phosphatase (ALP), alanine aminotransferase (ALT) in comparison with PBS group (Figure 2C,D). Hematoxylin and eosin (H&E) staining results revealed negligible damage on major organs including kidney, liver, spleen, and heart of mice treated with PThyN for two days

(Figure 2E). In clinic, high and repeated doses of iodinated contrast agents required to acquire contrast enhancement were reported to cause serious adverse effects and possible tissue damages.<sup>[22]</sup> These results point out that PThyN as novel contrast agents possess excellent biocompatibility, hemocompatibility, and systemic safety, facilitating its translational development.

#### 2.4. In Vivo Blood Pool CT Imaging

PThyN with a high iodine content of 49.2 wt% displayed strong signals on X-ray attenuation over a broad range of iodine concentrations from 2.5 to 50 mg mL<sup>-1</sup> (Figure 3A). Similar

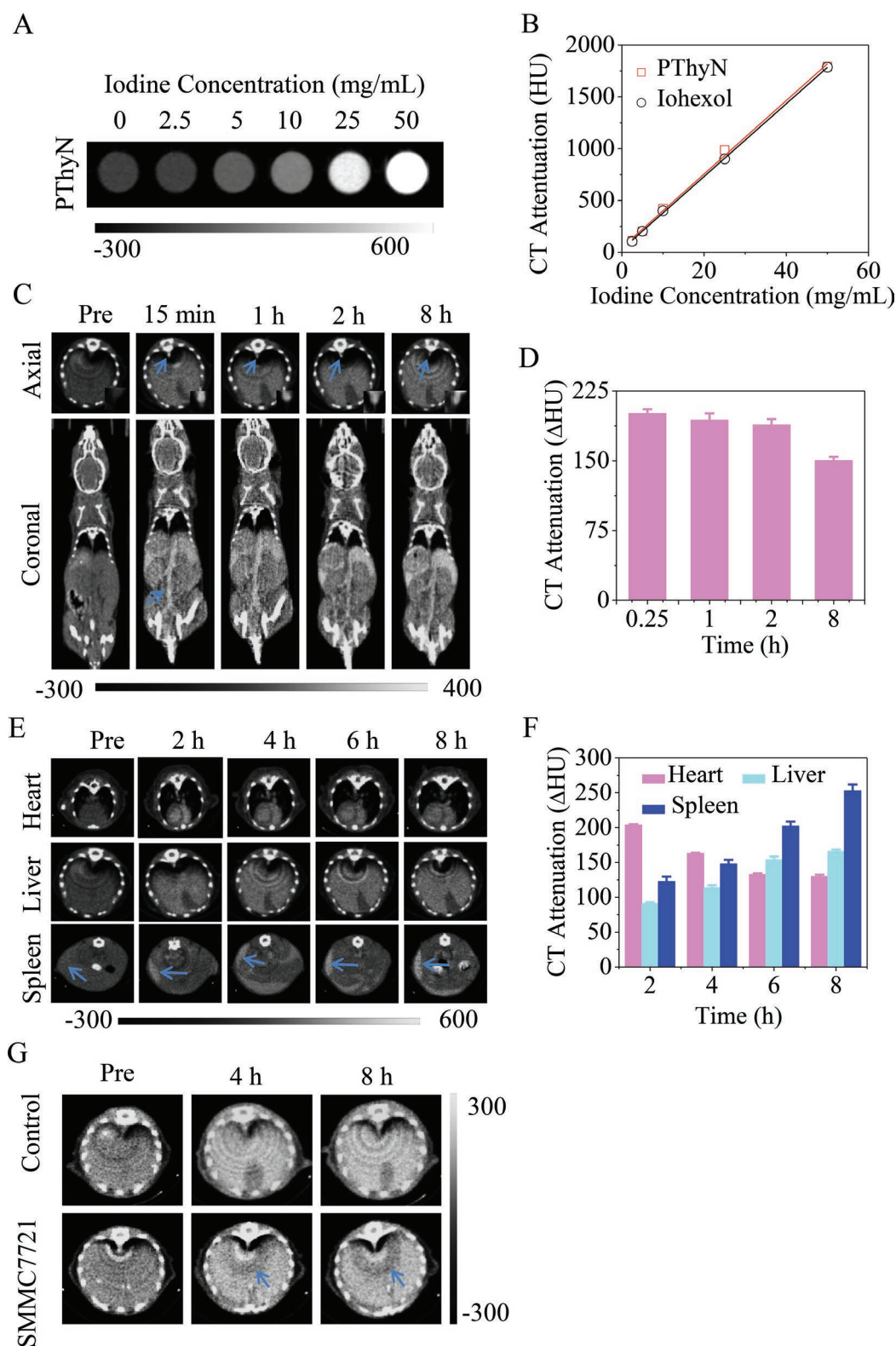


**Figure 3.** In vitro and in vivo blood pool CT imaging using PThyN as contrast agents. A) In vitro CT images of PThyN at different concentrations; B) dependence of X-ray attenuation efficacy of PThyN and iohexol on concentration; C) axial and coronal sections and D) dynamic contrast enhanced density ( $\Delta$ HU) of aorta of Balb/c mice i.v. treated with PThyN; E) in vivo CT images and F) dynamic contrast enhanced density ( $\Delta$ HU) of several major organs in Balb/c mice i.v. treated with PThyN; G) CT images of orthotopic SMMC-7721 liver tumor-bearing mice i.v. treated with PThyN. The i.v. injection dose of PThyN for in vivo imaging in inset (C–G) is fixed at 500 mg l equiv. per kg.

to clinically used iohexol, the attenuation signals of PThyN linearly increased with iodine concentrations (Figure 3B). Figure 3C revealed that Balb/c mice treated with PThyN at one single dose of 500 mg I equiv. per kg demonstrated clear delineation of both aorta and vena cava either from the coronal section or axial section, and had a remarkably enhanced contrast of aorta with a high  $\Delta$ HU value of around 200 in 15 min (Figure 3D). Remarkably, the CT signals of PThyN at aorta remained strong during the whole experimental period, and presented a high  $\Delta$ HU value of 150 even at 8 h postadministration. In contrast, iohexol at the same dose induced invisible contrast of vascular structure in mice (Figure S12, Supporting Information), owing to its fast renal clearance. Fenestra VC taken as a reference contrast agent for micro-CT often shows a clear blood pool imaging,<sup>[24]</sup> while suffers from a relatively large volume injection that would affect the cardiac and pulmonary functions.<sup>[25]</sup> Owing to the strong contrast of PThyN in the heart, the structure of cardiac ventricles was clearly delineated during the whole experimental period (Figure 3E). Although the CT attenuation signals decreased with time, the  $\Delta$ HU value at heart following 8 h postadministration was still higher than 125 (Figure 3F), signifying the tremendous potential of PThyN used as contrast agents for long-term imaging and online evaluation of cardiovascular diseases.

Taking advantage of passive accumulation to reticuloendothelial system, PThyN was employed for the delineation of liver and spleen. Significantly enhanced contrast was observed in liver and spleen following the administration of PThyN, and the CT signals increased with time in the initial 8 h (Figure 3E,F). As a result, lesions in liver and spleen could be visualized using PThyN as CT contrast agents. Figure 3G showed that orthotopic SMMC7721 liver cancer xenografts in mice following the intravenous injection of PThyN displayed a negative contrast of cancerous liver tissue that was devoid of reticuloendothelial system, while the control group demonstrated an entirely enhanced contrast within the healthy liver parenchyma. The damaged liver tissue in SMMC7721 liver cancer-bearing mice was also visualized through H&E staining assay (Figure S13, Supporting Information). Previously, ExiTron nano 6000 and Fenestra LC were observed to be effective iodinated nanocontrast agents for CT imaging of lesions in liver and spleen, including highly vascular hepatic metastasis.<sup>[26]</sup> It should be noted that PThyN accumulated in liver and spleen began to descend following 8 h postinjection, in which CT attenuation at spleen decreased from 234 at 8 h to 81 on day 30 (Figure S14, Supporting Information), indicating that PThyN was excreted with time. Thus, these iodinated nanoparticles could be superior nanocontrast agents for CT imaging of various diseases associated with aorta, heart, liver, and spleen.

## 2.5. In Vivo Tumor-Targeted CT Imaging in Subcutaneous B16F10 Melanoma and Orthotopic A549 Lung Tumor Xenografts

Contrast signals of PThyN in lesion sites including tumors could be conveniently boosted by facile incorporation of targeting ligands on the surface. cRGD peptide, a well-known targeting ligand, has been extensively employed to decorate

nanoparticles to enhance their cellular uptake in  $\alpha$ v $\beta$ 3 and  $\alpha$ v $\beta$ 5 integrin-overexpressing cancer cells.<sup>[27]</sup> Here, cRGD-decorated PThyN (cRGD-PThyN) developed from PEG-PThy and cRGD-PEG-PThy at a molar ratio of 4:1 was employed for in vivo CT imaging of different types of tumor xenografts. Subcutaneous B16F10 melanoma xenografts following the intratumoral injection of cRGD-PThyN at a single injection of 500 mg I equiv. per kg demonstrated remarkably enhanced contrast with a  $\Delta$ HU value of 430 in 5 min, and the CT attenuation signals although gradually decreasing with time were still higher than 240 at 4 h postinjection, signifying the enhanced CT contrast and prolonged retention of cRGD-PThyN in tumor sites (Figure 4A,B). On the other hand, iohexol exhibited swiftly decreasing CT contrast with a  $\Delta$ HU of 18 at 4 h, which was 13.3-fold lower than that of cRGD-PThyN. B16F10 melanoma tumor blocks were also imaged following i.v. injection of cRGD-PThyN. The results revealed that strong CT attenuation signal was visualized in tumor area of mice administered with cRGD-PThyN at the same dose (Figure 4C), and the  $\Delta$ HU value increased with time (Figure 4D). In particular, B16F10 melanoma displayed a significant CT attenuation signal of 82 HU at 8 h postadministration of cRGD-PThyN, which was 2.3-fold higher than that of PThyN, signifying the tumor selectivity and potent CT imaging of cRGD-PThyN.

Lung cancer is one of the leading causes of cancer death in the world, and thus its diagnosis is critical at the early stage and in the process of treatment. Here, we evaluated the CT imaging of A549 orthotopic lung tumor xenografts using cRGD-PThyN as contrast agents. The results demonstrated that significantly enhanced contrast either from the coronal section or axial section was observed in tumor-bearing mice following the administration with cRGD-PThyN at a single dose of 500 mg I equiv. per kg (Figure 4E). The quantitative analysis revealed that the  $\Delta$ HU value of orthotopic A549 tumor xenografts following the administration with cRGD-PThyN for 6 h was 115, which was in sharp contrast to the weak CT signal ( $\Delta$ HU = -250 HU) of pretreated tumor. These results signify that PThyN following the decoration with targeting ligands like cRGD has a great potential in the diagnosis of various  $\alpha$ v $\beta$ 3 and  $\alpha$ v $\beta$ 5 integrin-overexpressing tumors.

## 2.6. In Vivo SPECT/CT Imaging, Pharmacokinetics, and Biodistribution

Interestingly, PEG-PThy polymer could be easily labeled with radioactive <sup>125</sup>I by iodine exchange reaction with a high reaction efficiency of 56%, and the resulted <sup>125</sup>I-labeled polymer could similarly self-assemble into <sup>125</sup>I-labeled PThyN (<sup>125</sup>I-PThyN) for SPECT/CT imaging. Figure 5A demonstrates that <sup>125</sup>I-PThyN exhibited strong SPECT signals at <sup>125</sup>I concentrations of 10–160  $\mu$ Ci, and the signals linearly increased with increasing concentrations (Figure 5B), signifying its great potential as contrast agents of SPECT/CT imaging. Figure 5C showed enhanced contrast in the B16F10 tumors, confirms that <sup>125</sup>I-cRGD-PThyN could target to and accumulate in the tumors. Notably, the high SPECT/CT signals was observed at the tumor site for a long time, which is favorable for clinical diagnosis and therapy. More importantly, negligible SPECT signal was observed in the

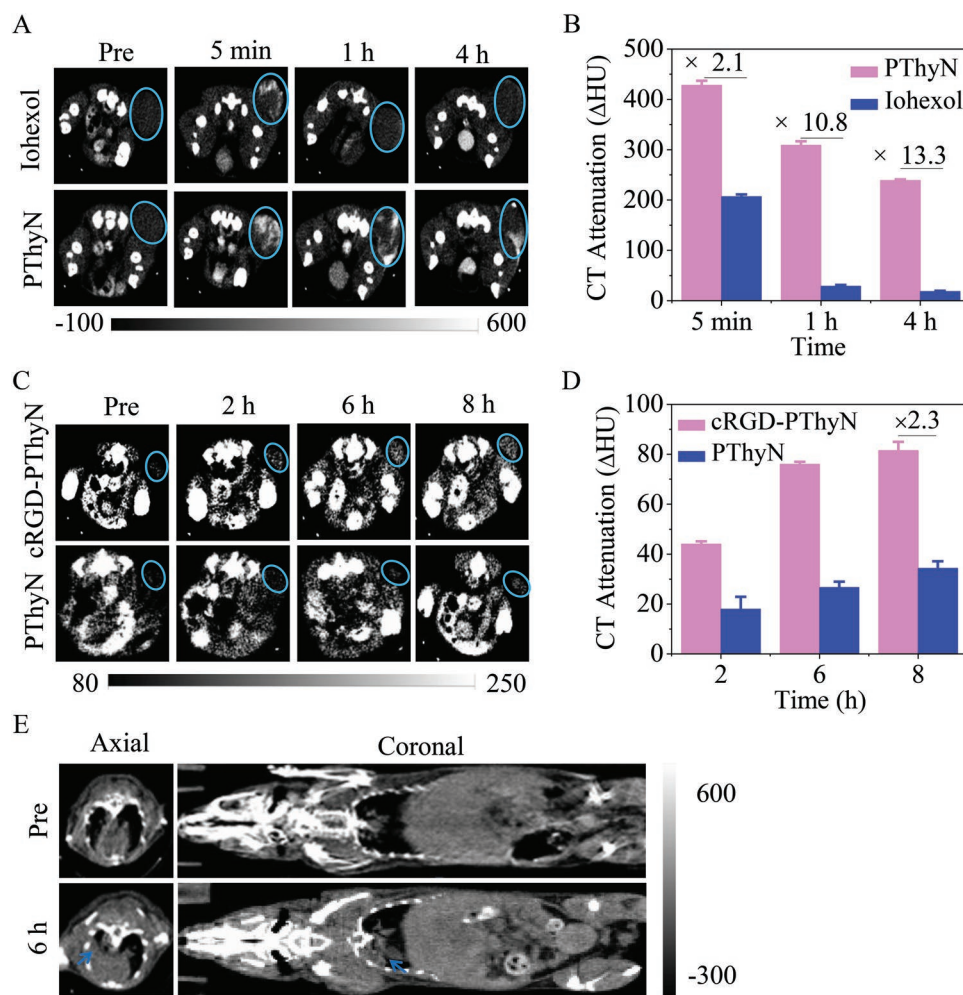


**Figure 4.** Active tumor-targeted CT imaging in subcutaneous B16F10 melanoma tumor and orthotopic human A549 tumor xenografts using cRGD-PThyN as contrast agents. A) In vivo CT images and B) dynamic contrast enhanced density ( $\Delta$ HU) of subcutaneous B16F10 mouse melanoma following intratumoral administration of cRGD-PThyN ( $500 \text{ mg l equiv. kg}^{-1}$ ). C) In vivo CT images and D) dynamic contrast enhanced density ( $\Delta$ HU) of subcutaneous B16F10 mouse melanoma tumor following i.v. administration of  $100 \mu\text{L}$  of PThyN and cRGD-PThyN at  $500 \text{ mg l equiv. per kg}$ . E) CT images of orthotopic A549 human lung tumor xenografts in mice i.v. treated with cRGD-PThyN ( $500 \text{ mg l equiv. per kg}$ ). Blue circled areas in insets (B) and (C) denote the enhanced contrast areas in the tumors.

thyroid of mice administrated with  $^{125}\text{I}$ -PThyN within 8 h, indicating that PThyN possesses high in vivo stability and unlikely induce iodine-provoked hyperthyroidism. Therefore, iodinated nanoparticles as dual-modal contrast agents could elegantly combine advantages of both SPECT (ultrahigh sensitivity) and CT (location of organs/tissues), providing better diagnosis of various diseases. In vivo pharmacokinetics was explored by detecting the  $^{125}\text{I}$  levels in plasma of mice following a single intravenous injection of  $^{125}\text{I}$ -PThyN and  $^{125}\text{I}$ -cRGD-PThyN. The results showed that nanoparticulate contrast agents had a long circulation time due to PEG shielding and decent sizes, in which substantial amount of  $^{125}\text{I}$  was still visualized even at 24 h following administration of  $^{125}\text{I}$ -PThyN and  $^{125}\text{I}$ -cRGD-PThyN (Figure 5D).  $^{125}\text{I}$ -cRGD-PThyN displayed a long elimination half-life ( $t_{1/2\beta}$ ) of 5.47 h, high area under the curve (AUC) of  $91.4 \text{ mg (L} \times \text{h)}^{-1}$ , slow clearance (CL) of  $9.03 \text{ L h}^{-1}$ , and relatively small volume of distribution ( $V_d$ ) of  $40.9 \text{ L}$  (Table S2, Supporting Information). In contrast, clinically used contrast

agents like iohexol and iodixanol generally present a short circulation time with an elimination phase half-life of several minutes.<sup>[28]</sup> The remarkably extended circulation time of PThyN would largely increase the temporal window for CT imaging of blood pool, and offer more accurate diagnosis of various diseases. Nanosized CT contrast agents based on nanoemulsions,<sup>[23,24]</sup> iodinated liposomes,<sup>[29]</sup> and polymeric nanoparticles<sup>[19c,21,30]</sup> have been explored and demonstrated prolonged blood circulation time as well as enhanced X-ray attenuation in vivo. At 8 h postinjection,  $^{125}\text{I}$ -cRGD-PThyN revealed a boosted tumor accumulation of 6.5% ID per gram, which was around 2.3 times higher than that of  $^{125}\text{I}$ -PThyN (Figure 5E). In particular, spleen and liver possessed highest accumulation of  $^{125}\text{I}$ -PThyN mainly due to the sequestration of reticuloendothelial system. Previous reports showed that nanoparticulate contrast agents based on polymethacrylate, polycarbonate, and polypeptide exhibited similar biodistribution.<sup>[19a,31]</sup> Meanwhile, a small amount of  $^{125}\text{I}$ -PThyN was observed in kidney during

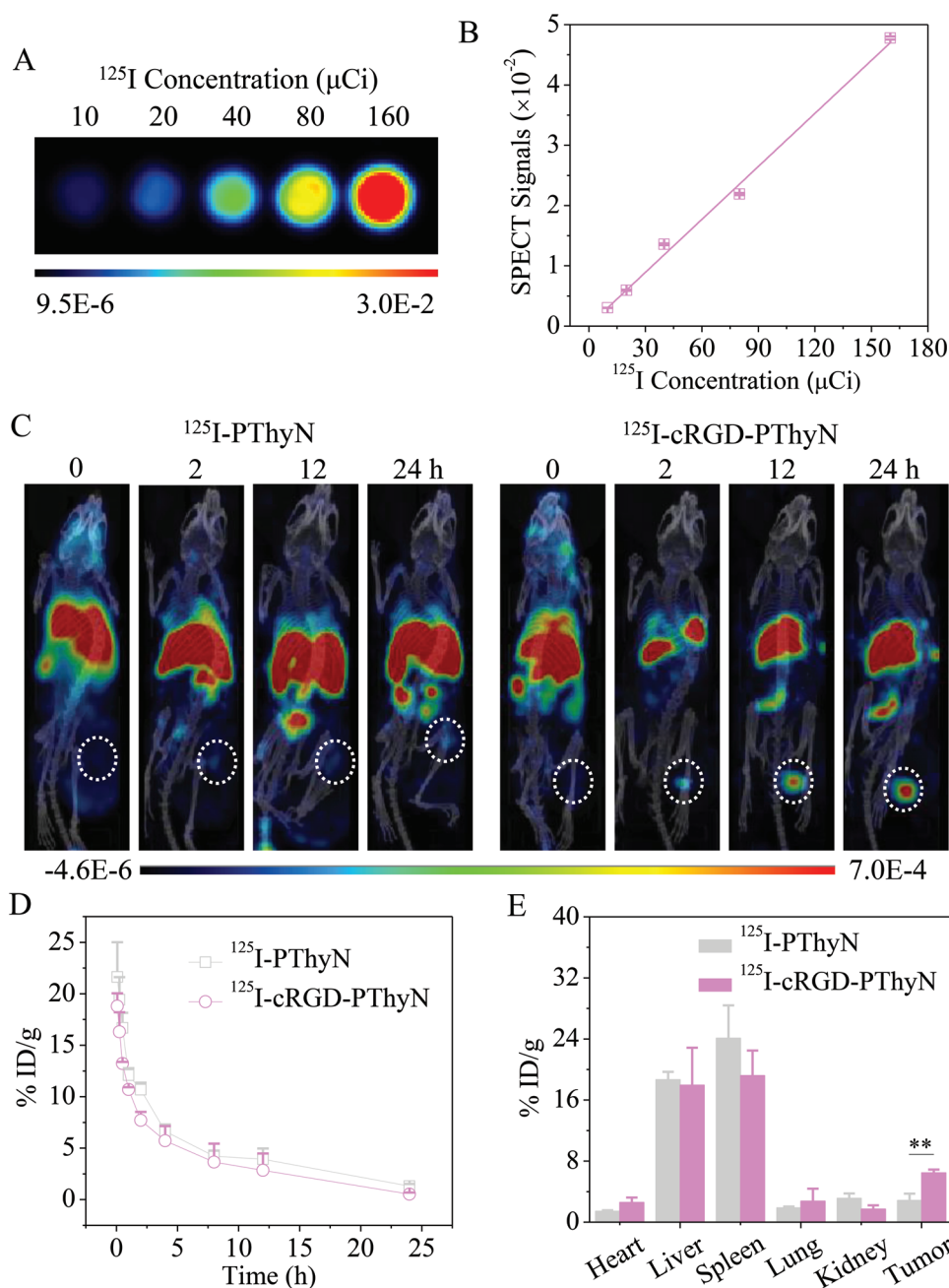


**Figure 5.** SPECT/CT imaging using  $^{125}\text{I}$ -PThyN as contrast agents. A) In vitro SPECT/CT imaging of  $^{125}\text{I}$ -PThyN at varying concentrations; B) dependence of SPECT signals of  $^{125}\text{I}$ -PThyN on concentrations; C) in vivo SPECT/CT imaging of Balb/c mice after i.v. injection of  $^{125}\text{I}$ -PThyN (left) and  $^{125}\text{I}$ -cRGD-PThyN (right) (108  $\mu\text{Ci}$ , 50 mg l equiv. per kg); D) in vivo pharmacokinetics of  $^{125}\text{I}$ -PThyN and  $^{125}\text{I}$ -cRGD-PThyN in Balb/c mice ( $n = 3$ ); E) quantification analysis of biodistribution in B16F10 tumor-bearing C57BL/6 mice treated with  $^{125}\text{I}$ -PThyN and  $^{125}\text{I}$ -cRGD-PThyN at 8 h post injection ( $n = 3$ ).

the whole experiment process, further corroborating the safety of PThyN toward kidney. In contrast, clinically used small molecular CT contrast agents often induce kidney lesion.

## 2.7. In Vivo Cancer Radiotherapy of $^{131}\text{I}$ -cRGD-PThyN

The in vivo antitumor efficacy of  $^{131}\text{I}$ -cRGD-PThyN was examined using B16F10 tumor-bearing mice. As shown in Figure 6A,

$^{131}\text{I}$ -cRGD-PThyN at a dose of 200  $\mu\text{Ci}$   $^{131}\text{I}$  per mouse remarkably suppressed tumor growth, in sharp contrast to PBS and cRGD-PThyN groups, which exhibited over 15-fold bigger tumor volume at 12 d postadministration. The photographs of tumor blocks harvested on day 12 verified that the tumor growth was nearly completely inhibited by  $^{131}\text{I}$ -cRGD-PThyN (Figure 6B).  $^{131}\text{I}$ -cRGD-PThyN displayed a tumor inhibition rate of 89.3% (Figure 6C), and induced no obvious body weight loss during the treatment period (Figure 6D), signifying its in

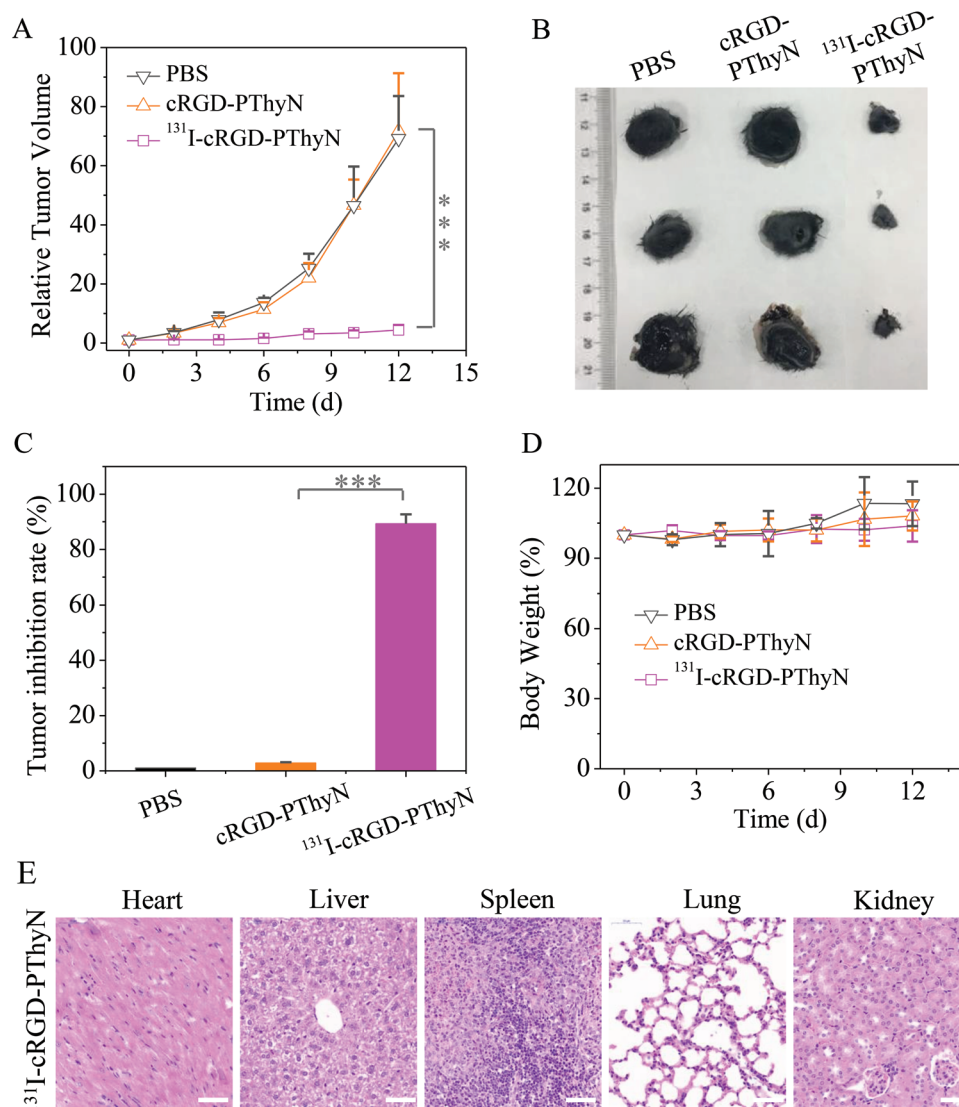


**Figure 6.** In vivo antitumor efficacy of <sup>131</sup>I-cRGD-PThyN in B16F10 melanoma-bearing C57BL/6 mice. The mice were i.v. administered with <sup>131</sup>I-cRGD-PThyN (200  $\mu$ Ci of <sup>131</sup>I per mouse), cRGD-PThyN and PBS on day 0, 3, 6, and 9. A) Tumor volume changes; B) photographs of tumor blocks on day 12 postadministration; C) tumor inhibition rate on day 12 postadministration; D) body weight changes ( $n = 5$ ,  $*p < 0.05$ ,  $**p < 0.01$ ,  $***p < 0.001$ ); E) histological analysis of the heart, liver, spleen, lung, and kidney of mice following 15 d treatment with <sup>131</sup>I-cRGD-PThyN. The images were obtained by a Leica microscope at magnification (40 $\times$ ). Scale bar: 200  $\mu$ m.

vivo safety. The promising therapeutic efficacy of <sup>131</sup>I-cRGD-PThyN to B16F10 tumor could be related to its significant tumor targeting ability and decent tumor penetration conferred by the relatively small size, as discussed in previous reports.<sup>[32]</sup> H&E histological analysis revealed that <sup>131</sup>I-cRGD-PThyN generated little damage to the heart, liver, spleen, lung, and kidney (Figure 6E; Figure S15, Supporting Information). Thus, cRGD-PThyN following the facile introduction of <sup>131</sup>I affords a potent nanoagent for cancer radiotherapy.

### 3. Conclusion

We have demonstrated that polypeptide-based nanoagents (PThyN) developed from PEG-PThyN can be employed for

versatile SPECT/CT dual-modality imaging and targeted radiotherapy in vivo. PThyN exhibits superb physicochemical properties including small size, high stability, iso-osmolality, low viscosity, and facile surface functionalization. Besides, PThyN displays excellent hematological and tissue compatibility. Taking advantages of a high iodine content of over 49.2 wt% and a long circulation time with an elimination half-life of 5.3 h, PThyN affords a remarkably extended and enhanced in vivo CT contrast to vascular system and soft tissues (heart, liver, spleen, etc.) following one single administration at a dose of 500 mg I equiv per kg. The nanoparticles can be easily decorated with different targeting ligands, and cRGD-functionalized PThyN (cRGD-PThyN) exhibits largely enhanced CT contrast in both subcutaneous B16F10 melanoma (>13-fold) and orthotopic A549 lung cancer in comparison with clinically used

iohexol. Meanwhile, the nanoparticles can be easily labeled with radioactive  $^{125}\text{I}$  for multiplexing imaging with CT (location of organs/tissues) and SPECT/CT (ultrahigh sensitivity), providing better diagnosis of major organs and monitoring of PThyN biodistribution in vivo. Besides,  $^{131}\text{I}$ -labeled and cRGD-functionalized PThyN displays over 89% tumor inhibition rate in B16F10 tumor in mice without causing significant adverse effects. Thus, PThyN featured with fascinating properties, great simplicity, good safety, and remarkable potency holds a tremendous potential on both diagnosis and therapy of varying diseases.

## 4. Experimental Section

**Synthesis of Thy-NCA:** Triphosgene (0.76 g, 2.6 mmol) was added to a solution of L-thyroxine (4.0 g, 5.2 mmol) in dry THF under  $\text{N}_2$  at  $50^\circ\text{C}$ . After stirring for 1 h, the reaction solution was concentrated, and then precipitated in excess petroleum ether to afford crude Thy-NCA. The crude product following dissolving in ethyl acetate was washed with cold saturated  $\text{NaHCO}_3$  aqueous solution and cold water sequentially, and dried with anhydrous  $\text{MgSO}_4$ . After removing the solvent by rotary evaporation, the product was dried under high vacuum for 24 h. Yield: 80.0%.  $^1\text{H}$  NMR ( $\text{DMSO}-d_6$ , 400 MHz, Figure S1 (Supporting Information),  $\delta$ ): 9.27 (s, 1H,  $-\text{OH}$ ), 9.15 (s, 1H,  $-\text{CONH}$ ), 7.83 (s, 2H,  $-\text{C}_6\text{H}_2\text{OH}$ ), 7.10 (s, 2H,  $-\text{C}_6\text{H}_2\text{O}$ ), 4.79 (t, 1H,  $-\text{CHNH}$ ), 2.98–3.08 (d, 2H,  $-\text{C}_6\text{H}_2\text{CH}_2\text{CH}-$ ).  $^{13}\text{C}$  NMR ( $\text{DMSO}-d_6$ , 100 MHz, Figure S2 (Supporting Information),  $\delta$ ): 171.06, 152.30, 152.15, 151.37, 150.57, 141.41, 137.68, 125.47, 92.41, 88.11, 58.35, 35.15. Anal. Calcd for  $\text{C}_{16}\text{H}_9\text{I}_4\text{NO}_5$ : C, 23.91; H, 1.12; N, 1.74. Found: C, 24.05; H, 1.31; N, 1.92. Electrospray ionization mass spectrometry (ESI-MS,  $m/z$ ): calcd for  $\text{C}_{16}\text{H}_9\text{I}_4\text{NO}_5$  802.6; found 802.6.

**Preparation of mPEG-PThy and cRGD-PEG-PThy Copolymers:** mPEG-PThy copolymers were synthesized by ring-opening polymerization of Thy-NCA monomer in  $N,N$ -dimethylformamide (DMF) using mPEG-NH $_2$  ( $M_n = 3.0 \text{ kg mol}^{-1}$ ) as an initiator. Typically, to a solution of LT-NCA (1.2 g, 1.5 mmol) in DMF (6.0 mL) was rapidly added a stock solution of mPEG-NH $_2$  (300 mg, 0.1 mmol) in DMF (6.0 mL). After stirring at  $40^\circ\text{C}$  under  $\text{N}_2$  for 72 h, the product was recovered through precipitation in ethyl ether and drying under high vacuum for 24 h. Yield: 76.0%.  $^1\text{H}$  NMR (400 MHz,  $\text{DMSO}-d_6$ , Figure S3 (Supporting Information),  $\delta$ ): 9.24 ( $-\text{OH}$ ), 8.35 ( $-\text{CONH}-$ ), 7.66–7.84 ( $-\text{C}_6\text{H}_2\text{OH}$ ), 7.06–7.12 ( $-\text{C}_6\text{H}_2\text{O}$ ), 4.15 ( $-\text{COCHNH}-$ ), 3.51 ( $-\text{OCH}_2\text{CH}_2\text{O}-$ ), 3.24 ( $-\text{OCH}_3$ ), 2.83 ( $-\text{C}_6\text{H}_2\text{CH}_2\text{CH}-$ ). Similarly, maleimide-functionalized PEG-PThy (Mal-PEG-PThy) was acquired by polymerization of Thy-NCA monomer using Mal-PEG-NH $_2$  ( $M_n = 4.0 \text{ kg mol}^{-1}$ ) as an initiator. Then, a solution of Mal-PEG-PThy (115.9 mg, 0.01 mmol Mal group) in DMF (5.0 mL) was added to a solution of cyclic RGDfC peptide (cRGD, 9.8 mg, 0.012 mmol) in DMF (1 mL). The reaction proceeded at r.t. for 24 h. The product was purified by exhaustive dialysis (MWCO 7000) in D.I. water followed by lyophilization to obtain cRGD-PEG-PThy. Yield: 70.0%. The degree of cRGD conjugation was calculated by measuring the arginine content using the 9,10-phenanthrene-quinone technique.

**Preparation of PThyN and cRGD-PThyN:** PThyN were constructed by dropwise addition of 4.0 mL of phosphate buffer (PB, pH 7.4,  $10 \times 10^{-3} \text{ M}$ ) to a DMF solution of PEG-PThy (5.0 mg  $\text{mL}^{-1}$ , 1.0 mL) under stirring at r.t. followed by extensive dialysis against PB for 12 h using a membrane (MWCO 7000 Da). cRGD-PThyN was similarly fabricated except that a mixture of cRGD-PEG-PThy and PEG-PThy at a molar ratio of 1:4 was employed. The size and colloidal stability of PThyN against extensive dilution and 10% FBS were determined by DLS.

**In Vitro CT Imaging:** All the samples were scanned on a U-SPECT/CT system (MILabs, Netherlands), and the images were acquired at an X-ray voltage of 55 kVp, an anode current of 615  $\mu\text{A}$  accurate mode using full angle with three frame averaging. The concentrations of PThyN were 2.5, 5, 10, 25, and 50 mg  $\text{mL}^{-1}$ . Deionized water (0 HU) was used as a control.

**Blood and Histological Analysis:** All animal experiments were approved by the Animal Care and Use Committee of Soochow University, and all protocols of animal studies conformed to the Guide for the Care and Use of Laboratory Animals. The in vivo biocompatibility and safety of PThyN were evaluated by blood and histological analysis in healthy mice following the injection of 200  $\mu\text{L}$  of PThyN at a dose of 500 mg  $\text{I equiv. per kg}$ . For blood analysis, mice were sacrificed 2 d postinjection, and blood parameters (WBC, RBC, HGB, HCT, MCH, MCHC, MCV, PLT, RDW, MPV, etc.), blood biochemistry (AST, ALP, ALT, ALB) were analyzed.

Following the injection of PThyN at a dose of 500 mg  $\text{I equiv. per kg}$  for 2 d, the Balb/c mice ( $n = 3$ ) were sacrificed under anesthetic conditions. Major organs including lung, kidney, liver, spleen, and heart were harvested and fixed with neutral buffered formalin (NBF, 10%). Then, the fixed organ tissues were embedded into paraffin, sectioned into slices with 4  $\mu\text{m}$  thickness, stained with hematoxylin and eosin (H&E), and then observed using a digital microscope (Leica QWin).

**In Vivo CT Imaging of Blood Pool and Different Tumors:** The in vivo CT imaging of blood pool using PThyN as contrast agents was performed in Balb/c nude mice (18–22 g). 200  $\mu\text{L}$  of PThyN at a dosage of 500 mg  $\text{I equiv. kg}^{-1}$  was intravenously administered via tail vein, and the CT imaging was performed using U-SPECT/CT system (MILabs, Netherlands) as described above at 0.25, 1, 2, or 8 h postinjection. Iohexol was used as a control.

The in vivo CT imaging of tumors using cRGD-PThyN was studied in tumor-bearing mice. The malignant B16F10 tumor model was established by subcutaneously injecting 50  $\mu\text{L}$  of B16F10 cells ( $8 \times 10^6$ ) in serum-free DMEM media to the hind flank of C57BL/6 mice. A549 orthotopic lung tumor model was acquired by injecting A549-Luc cells ( $5 \times 10^6$ ) mixed in 100  $\mu\text{L}$  of PBS/matrigel (4/1, v/v) into the left lung parenchyma of nude mice. For CT imaging, PThyN with a dose of 500 mg  $\text{I equiv. per kg}$  was administered either via intratumoral or intravenous injection. CT photographs were acquired at 2, 4, 6, and 8 h postinjection.

**In Vivo SPECT/CT Imaging:** For in vivo SPECT/CT imaging,  $^{125}\text{I}$ -bearing PThyN ( $^{125}\text{I}$ -PThyN) was prepared from  $^{125}\text{I}$ -labeled PEG-PThy copolymer that was obtained by iodine exchange reaction of PEG-PThy (2 mg) with  $\text{Na}^{125}\text{I}$  in DMF (216  $\mu\text{Ci}$ , 200  $\mu\text{L}$ ) at  $80^\circ\text{C}$  for 8 h. Excess  $\text{Na}^{125}\text{I}$  in  $^{125}\text{I}$ -PThyN solution was removed by extensive dialysis against PB (pH 7.4,  $10 \times 10^{-3} \text{ M}$ ) for 10 h using a dialysis bag (MWCO 7000 Da). The radioactivity of  $^{125}\text{I}$ -PThyN was measured by radioactivity meter (Beijing Heng Odd Instrument Co., Ltd). The efficiency of iodine exchange reaction determined by the radioactivity ratio of  $^{125}\text{I}$ -PThyN to the initial radioactivity of  $\text{Na}^{125}\text{I}$  was 56%. 200  $\mu\text{L}$  of  $^{125}\text{I}$ -PThyN (108  $\mu\text{Ci}$ ) was i.v. administered into B16F10 tumor-bearing C57BL/6 mice, and the SPECT/CT photographs were collected using U-SPECT/CT (MILabs, Netherlands).

**Blood Circulation and Biodistribution:** To investigate the blood circulation of PThyN,  $^{125}\text{I}$ -PThyN, and  $^{125}\text{I}$ -cRGD-PThyN were injected into Balb/c mice via tail vein at a  $^{125}\text{I}$  concentration of 50  $\mu\text{Ci kg}^{-1}$ , around 50  $\mu\text{L}$  of blood was withdrawn from the orbit of mice at predetermined time points. The  $^{125}\text{I}$  level of the blood samples was acquired by radioactivity measurement. The distribution half-life ( $t_{1/2\alpha}$ ),  $t_{1/2\beta}$ , AUC,  $V_d$ , and CL were calculated by fitting the blood drug pharmaceutical concentrations to a two compartment model using EXCEL.

To evaluate the biodistribution,  $^{125}\text{I}$ -PThyN and  $^{125}\text{I}$ -cRGD-PThyN were injected into B16F10 tumor-bearing C57BL/6 mice via tail vein at a  $^{125}\text{I}$  concentration of 50  $\mu\text{Ci kg}^{-1}$ . At 8 h after injection, the mice were sacrificed. The major organs and tumors were collected, and the  $^{125}\text{I}$  level in the organs and tumors was acquired by radioactivity measurement.

**In Vivo Radiotherapy:** Mice bearing subcutaneous B16F10 melanoma tumors were divided into three groups ( $n = 5$ ). When the tumors reached around 50  $\text{mm}^3$ , the mice were i.v. administered with PBS, cRGD-PThyN (200  $\mu\text{L}$ , 50 mg  $\text{I equiv./kg}$ ), or  $^{131}\text{I}$ -cRGD-PThyN (200  $\mu\text{Ci}$ , 200  $\mu\text{L}$ , 50 mg  $\text{I equiv. per kg}$ ) on day 0, 3, 6, and 9. The tumor volume was measured and normalized by the initial tumor volume.

## Supporting Information

Supporting Information is available from the Wiley Online Library or from the author.

## Acknowledgements

This work was supported by the National Natural Science Foundation of China (NSFC 51773145, 51473110, and 51633005).

## Conflict of Interest

The authors declare no conflict of interest.

## Keywords

CT imaging, polypeptides, radiotherapy, SPECT imaging, theranostic agents

Received: May 17, 2019

Revised: August 8, 2019

Published online:

- [1] a) H. Chen, W. Zhang, G. Zhu, J. Xie, X. Chen, *Nat. Rev. Mater.* **2017**, 2, 17024; b) S. Kunjachan, J. Ehling, G. Storm, F. Kiessling, T. Lammers, *Chem. Rev.* **2015**, 115, 10907; c) G. Chen, I. Roy, C. Yang, P. N. Prasad, *Chem. Rev.* **2016**, 116, 2826; d) Z. Tang, C. He, H. Tian, J. Ding, B. S. Hsiao, B. Chu, X. Chen, *Prog. Polym. Sci.* **2016**, 60, 86.
- [2] a) T.-H. Shin, Y. Choi, S. Kim, J. Cheon, *Chem. Soc. Rev.* **2015**, 44, 4501; b) X. Li, J. Kim, J. Yoon, X. Chen, *Adv. Mater.* **2017**, 29, 1606857; c) M. Baues, A. Dasgupta, J. Ehling, J. Prakash, P. Boor, F. Tacke, F. Kiessling, T. Lammers, *Adv. Drug Delivery Rev.* **2017**, 121, 9; d) X. Jiang, S. Zhang, F. Ren, L. Chen, J. Zeng, M. Zhu, Z. Cheng, M. Gao, Z. Li, *ACS Nano* **2017**, 11, 5633.
- [3] a) G. Mariani, L. Bruselli, T. Kuwert, E. E. Kim, A. Flotats, O. Israel, M. Dondi, N. Watanabe, *Eur. J. Nucl. Med. Mol. Imaging* **2010**, 37, 1959; b) R. J. Hicks, M. S. Hofman, *Nat. Rev. Clin. Oncol.* **2012**, 9, 712.
- [4] A. Flotats, J. Knuuti, M. Gutberlet, C. Marcassa, F. M. Bengel, P. A. Kaufmann, M. R. Rees, B. Hesse, *Eur. J. Nucl. Med. Mol. Imaging* **2011**, 38, 201.
- [5] a) A. M. Avram, *J. Nucl. Med.* **2012**, 53, 754; b) Y. Maruoka, K. Abe, S. Baba, T. Isoda, H. Sawamoto, Y. Tanabe, M. Sasaki, H. Honda, *Radiology* **2012**, 265, 902; c) Y.-X. Mi, X. Sui, J.-M. Huang, L.-G. Wei, P. Xie, *Medicine* **2017**, 96, e8348.
- [6] a) I. M. C. van der Ploeg, R. A. V. Olmos, O. E. Nieweg, E. J. T. Rutgers, B. B. Kroon, C. A. Hoefnagel, *J. Nucl. Med.* **2007**, 48, 1756; b) L. Vermeeren, I. M. C. Van Der Ploeg, R. A. V. Olmos, W. Meinhart, W. M. C. Klop, B. B. R. Kroon, O. E. Nieweg, *J. Surg. Oncol.* **2010**, 101, 184.
- [7] a) E. B. Ehlerding, P. Grodzinski, W. Cai, C. H. Liu, *ACS Nano* **2018**, 12, 2106; b) P. U. Atukorale, G. Covarrubias, L. Bauer, E. Karathanasis, *Adv. Drug Delivery Rev.* **2017**, 113, 141.
- [8] a) S. Zhang, C. Sun, J. Zeng, Q. Sun, G. Wang, Y. Wang, Y. Wu, S. Dou, M. Gao, Z. Li, *Adv. Mater.* **2016**, 28, 8927; b) Y. Wang, Y. Wu, Y. Liu, J. Shen, L. Lv, L. Li, L. Yang, J. Zeng, Y. Wang, L. W. Zhang, Z. Li, M. Gao, Z. Chai, *Adv. Funct. Mater.* **2016**, 26, 5335.
- [9] X. Li, C. Wang, H. Tan, L. Cheng, G. Liu, Y. Yang, Y. Zhao, Y. Zhang, Y. Li, C. Zhang, Y. Xiu, D. Cheng, H. Shi, *Biomaterials* **2016**, 108, 71.
- [10] Y. Wu, Y. Sun, X. Zhu, Q. Liu, T. Cao, J. Peng, Y. Yang, W. Feng, F. Li, *Biomaterials* **2014**, 35, 4699.
- [11] a) B. Zhou, R. Wang, F. Chen, L. Zhao, P. Wang, X. Li, I. Banyai, Q. Ouyang, X. Shi, M. Shen, *ACS Appl. Mater. Interfaces* **2018**, 10, 6146; b) X. Li, Z. Xiong, X. Xu, Y. Luo, C. Peng, M. Shen, X. Shi, *ACS Appl. Mater. Interfaces* **2016**, 8, 19883.
- [12] a) G. Song, L. Cheng, Y. Chao, K. Yang, Z. Liu, *Adv. Mater.* **2017**, 29, 1700996; b) S. Goel, D. Ni, W. Cai, *ACS Nano* **2017**, 11, 5233.
- [13] a) X. Yi, K. Yang, C. Liang, X. Zhong, P. Ning, G. Song, D. Wang, C. Ge, C. Chen, Z. Chai, Z. Liu, *Adv. Funct. Mater.* **2015**, 25, 4689; b) S. Liang, X. Jin, Y. Ma, J. Guo, H. Wang, *RSC Adv.* **2015**, 5, 88560.
- [14] a) S. Her, D. A. Jaffray, C. Allen, *Adv. Drug Delivery Rev.* **2017**, 109, 84; b) M. Laprise-Pelletier, T. Simao, M.-A. Fortin, *Adv. Healthcare Mater.* **2018**, 7, 1701460.
- [15] B. M. Casey, E. A. Thom, A. M. Peaceman, M. W. Varner, Y. Sorokin, D. G. Hirtz, U. M. Reddy, R. J. Wapner, J. M. Thorp Jr., G. Saade, A. T. N. Tita, D. J. Rouse, B. Sibai, J. D. Iams, B. M. Mercer, J. Tolosa, S. N. Caritis, J. P. VanDorsten, *N. Engl. J. Med.* **2017**, 376, 815.
- [16] a) L. Chen, X. Zhong, X. Yi, M. Huang, P. Ning, T. Liu, C. Ge, Z. Chai, Z. Liu, K. Yang, *Biomaterials* **2015**, 66, 21; b) J. Cao, Y. Wei, Y. Zhang, G. Wang, X. Ji, Z. Zhong, *ACS Appl. Mater. Interfaces* **2019**, 11, 18953.
- [17] a) H. Cabral, K. Miyata, K. Osada, K. Kataoka, *Chem. Rev.* **2018**, 118, 6844; b) Z. Song, Z. Han, S. Lv, C. Chen, L. Chen, L. Yin, J. Cheng, *Chem. Soc. Rev.* **2017**, 46, 6570; c) T. J. Deming, *Chem. Rev.* **2016**, 116, 786; d) C. Deng, J. Wu, R. Cheng, F. Meng, H.-A. Klok, Z. Zhong, *Prog. Polym. Sci.* **2014**, 39, 330; e) C. He, X. Zhuang, Z. Tang, H. Tian, X. Chen, *Adv. Healthcare Mater.* **2012**, 1, 48.
- [18] N. Graf, D. R. Bielenberg, N. Kolishetti, C. Muus, J. Banyard, O. C. Farokhzad, S. J. Lippard, *ACS Nano* **2012**, 6, 4530.
- [19] a) V. P. Torchilin, M. D. Frank-Kamenetsky, G. L. Wolf, *Acad. Radiol.* **1999**, 6, 61; b) P. Ghosh, M. Das, A. P. Rameshbabu, D. Das, S. Datta, S. Pal, A. B. Panda, S. Dhara, *ACS Appl. Mater. Interfaces* **2014**, 6, 17926; c) Q. Yin, F. Y. Yap, L. C. Yin, L. Ma, Q. Zhou, L. W. Dobrucki, T. M. Fan, R. C. Gaba, J. J. Cheng, *J. Am. Chem. Soc.* **2013**, 135, 13620; d) Y. Q. Zhu, X. X. Wang, J. Chen, J. Zhang, F. H. Meng, C. Deng, R. Cheng, F. J. Jan, Z. Y. Zhong, *J. Controlled Release* **2016**, 244, 229.
- [20] a) Y. Shi, R. van der Meel, B. Theek, E. O. Blenke, E. H. E. Pieters, M. H. A. M. Fens, J. Ehling, R. M. Schifferers, G. Storm, C. F. van Nostrum, T. Lammers, W. E. Hennink, *ACS Nano* **2015**, 9, 3740; b) K. Liang, J. E. Chung, S. J. Gao, N. Yongvongsontorn, M. Kurisawa, *Adv. Mater.* **2018**, 30, 1706963; c) X. Wei, Y. Wang, X. Xiong, X. Guo, L. Zhang, X. Zhang, S. Zhou, *Adv. Funct. Mater.* **2016**, 26, 8266; d) X. Gu, M. Qiu, H. Sun, J. Zhang, L. Cheng, C. Deng, Z. Zhong, *Biomater. Sci.* **2018**, 6, 1526.
- [21] S. You, H.-y. Jung, C. Lee, Y. H. Choe, J. Y. Heo, G.-T. Gang, S.-K. Byun, W. K. Kim, C.-H. Lee, D.-E. Kim, Y. I. Kim, Y. Kim, *J. Controlled Release* **2016**, 226, 258.
- [22] J. C. De La Vega, U. O. Hafeli, *Contrast Media Mol. Imaging* **2015**, 10, 81.
- [23] a) A. de Vries, E. Custers, J. Lub, S. van den Bosch, K. Nicolay, H. Grull, *Biomaterials* **2010**, 31, 6537; b) M. F. Attia, N. Anton, M. Chipier, R. Akasov, H. Anton, N. Messaddeq, S. Fournel, A. S. Klymchenko, Y. Mely, T. F. Vandamme, *ACS Nano* **2014**, 8, 10537.
- [24] X. Li, N. Anton, G. Zuber, M. J. Zhao, N. Messaddeq, F. Hallouard, H. Fessi, T. F. Vandamme, *Biomaterials* **2013**, 34, 481.
- [25] C. E. Suckow, D. B. Stout, *Mol. Imaging Biol.* **2008**, 10, 114.
- [26] a) H. W. Kim, Q.-Y. Cai, H. Y. Jun, K. S. Chon, S. H. Park, S. J. Byun, M. S. Lee, J. M. Oh, H. S. Kim, K.-H. Yoon, *Acad. Radiol.* **2008**,

- 15, 1282; b) H. Boll, S. Nittka, F. Doyon, M. Neumaier, A. Marx, M. Kramer, C. Groden, M. A. Brockmann, *PLoS One* **2011**, 6, e25692.
- [27] a) H. Chen, G. Niu, H. Wu, X. Chen, *Theranostics* **2016**, 6, 78; b) M. Qiu, J. Ouyang, H. Sun, F. Meng, R. Cheng, J. Zhang, L. Cheng, Q. Lan, C. Deng, Z. Zhong, *ACS Appl. Mater. Interfaces* **2017**, 9, 27587; c) S. Quader, X. Liu, Y. Chen, P. Mi, T. Chida, T. Ishii, Y. Miura, N. Nishiyama, H. Cabral, K. Kataoka, *J. Controlled Release* **2017**, 258, 56.
- [28] Q. Y. Cai, S. H. Kim, K. S. Choi, S. Y. Kim, S. J. Byun, K. W. Kim, S. H. Park, S. K. Juhng, K. H. Yoon, *Invest. Radiol.* **2007**, 42, 797.
- [29] a) D. B. Elrod, R. Partha, D. Danila, S. W. Casscells, J. L. Conyers, *Nanomed. Nanotechnol.* **2009**, 5, 42; b) S. N. Ekdawi, J. M. P. Stewart, M. Dunne, S. Stapleton, N. Mitsakakis, Y. N. Dou, D. A. Jaffray, C. Allen, *J. Controlled Release* **2015**, 207, 101.
- [30] a) W. H. Kong, W. J. Lee, Z. Y. Cui, K. H. Bae, T. G. Park, J. H. Kim, K. Park, S. W. Seo, *Biomaterials* **2007**, 28, 5555; b) H. K. Gaikwad, D. Tsvirkun, Y. Ben-Nun, E. Merquirol, R. Popovtzer, G. Blum, *Nano Lett.* **2018**, 18, 1582.
- [31] a) Y. Zou, Y. H. Wei, G. L. Wang, F. H. Meng, M. Y. Gao, G. Storm, Z. Y. Zhong, *Adv. Mater.* **2017**, 29, 1603997; b) J. Wallyn, N. Anton, C. A. Serra, M. Bouquey, M. Collot, H. Anton, J.-L. Weickert, N. Messaddeq, T. F. Vandamme, *Acta Biomater.* **2018**, 66, 200.
- [32] a) Q. Sun, T. Ojha, F. Kiessling, T. Lammers, Y. Shi, *Biomacromolecules* **2017**, 18, 1449; b) K. Huang, Y. He, Z. Zhu, J. Guo, G. Wang, C. Deng, Z. Zhong, *ACS Appl. Mater. Interfaces* **2019**, 11, 22171.